Accepted Manuscript

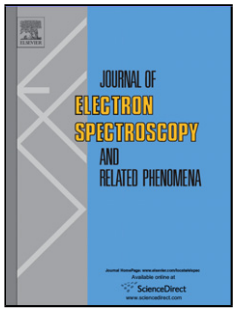

Title: Structure stability of free copper nanoclusters: FSA-DFT Cu-building and FDM-XANES study

Authors: Leandro Andrini, Germán J. Soldano, Marcelo M. Mariscal, Félix G. Requejo, Yves Joly

PII: S0368-2048(18)30251-2
DOI: https://doi.org/10.1016/j.elspec.2019.05.005
Reference: ELSPEC 46856

To appear in: *Journal of Electron Spectroscopy and Related Phenomena*

Received date: 22 November 2018
Revised date: 10 May 2019
Accepted date: 15 May 2019

Please cite this article as: Andrini L, Soldano GJ, Mariscal MM, Requejo FG, Joly Y, Structure stability of free copper nanoclusters: FSA-DFT Cu-building and FDM-XANES study, *Journal of Electron Spectroscopy and Related Phenomena* (2019), https://doi.org/10.1016/j.elspec.2019.05.005

Structure stability of free copper nanoclusters: FSA-DFT Cu-building and FDM-XANES study

Leandro Andrini[a]*, Germán J. Soldano[b]*, Marcelo M. Mariscal[b], Félix G. Requejo[ac] and Yves Joly[d]

a. Instituto de Fisicoquímica Teórica y Aplicada, Dto. de Química, Facultad de Ciencias Exactas, Universidad Nacional de La Plata, (INIFTA/ UNLP-CONICET La Plata), Diag. 113 y 64, La Plata, Buenos Aires, 1900, Argentina

b. INFIQC, CONICET. Departamento de Química Teórica y Computacional, Facultad de Ciencias Químicas, Universidad Nacional de Córdoba, Medina Allende y Haya de la Torre, Córdoba, Córdoba, X5000HUA, Argentina

c. Departamento de Física, Fac. de Ciencias Exactas, Universidad Nacional de La Plata., 49 y 115, La Plata, Buenos Aires, 1900, Argentina

d. Université Grenoble Alpes, CNRS, Grenoble INP, Institut Néel, 25 rue des Martyrs BP 166, Grenoble, 38042, France

* Correspondence email: andrini@inifta.unlp.edu.ar; german.soldano@unc.edu.ar

Highlights

- Theoretical study combined DFT + XANES simulations
- Electronic and morphological structures of Cu20 clusters
- New properties of transition metal clusters

Abstract We present ab initio simulations of X-ray Absorption Near-Edge Structure (XANES) spectra, performed on model clusters built by fast simulated annealing and optimized by Density Functional Theory (DFT) minimization. As is known, larger stability of Cu clusters with 20 atoms was found in comparison with those with 19 and 21 atoms. Based on this knowledge, we show the sensitivity of the XANES technique on the number of atoms *n*, (c.a 20), and on the morphology of the Cu_n nanoclusters. For this study we used both L3 and K edges and found the former more sensitive. In addition, in the case of the K XANES edge, we carry out the simulations using four different methods, to observe their performance in arrays of a few atoms. Even more, we obtain a good agreement between our results and previous predictions on the HOMO-LUMO gaps for these systems.

Keywords: Cu-Clusters; FSA-DFT; XANES; FDMNES-code.

1. Introduction

While the speculation concerning the behaviour of matter at a scale of a few atoms crosses the history of human thought, the scientific study of atomic clusters is recent, since the last two decades of the twentieth century (Johnston, 2002). From those years, considerable progress in the knowledge of these systems were done (Shao *et al.*, 2006; Kaldor *et al.*, 2009; Jena, 2013), but due to production and characterization difficulties, many questions remain opened. It can be said that the studies of clusters are divided into four main stages: *calculus* methods and theoretical cluster predictions (Wales & Doye, 1997; Wales & Scheraga, 1999; Darby *et al.*, 2002), physical-chemistry cluster generation (Wang & Herron, 1991; Alivisatos, 1996), cluster detection (Kneipp *et al.*, 1997; Haes *et al.*, 2005; Xie *et al.*, 2009), and cluster experiments where the cluster are probed in its applications and tested with multiple techniques (Toshima & Yonezawa, 1998; Kim *et al.*, 2002; Sönnichsen *et al.*, 2002). The involved cluster sizes, ranging from some atoms and the nano-meter radius (Vilar- Vidal *et al.*, 2014) up, to some millions of atoms (Johnston, 2002), make their evidence at the limit of the detection techniques (Smeeton *et al.*, 2003).

Another aspect is that, copper nanoclusters (Cu-NCs), for example, are difficult to stabilize because of atom-specific electron configuration (Oyanagi *et al.*, 2014), in contrast with intermetallic, such as Au_mAg_n or Au_mCu_n isolable, which are monodisperse and with atomically precise nature (Nguyen *et al.*, 2015). Previous attempts to generate large Cu-NCs have produced ill-defined mixtures, or required the use of cryogenic matrices (Apai *et al.*, 1979; Soldatov *et al.*, 2006; Nguyen *et al.*, 2015). The isolation of atomically precise copper nanoclusters would be a significant advance, since they could address important unanswered questions, for example in catalytic activities (Schouten *et al.*, 2012; Calle- Vallejo & Koper, 2013; Nguyen *et al.*, 2015). The study of free clusters is not straightforward because of the difficulty to measure the physical properties of single particles, or due to the presence of isomers with close energies and low interconversion barriers. Consequently, measured properties cannot correspond to the assigned configuration (Garzón *et al.*, 1998; Wang *et al.*, 2002; Johnston, 2002). Anyway, the promising expected technological applications of nano-particles require improved descriptions of these systems (Vilar-Vidal *et al.*, 2010; Santiago González *et al.*, 2010).

The disciplinary beginning of the physics and chemistry of clusters was theoretical speculations (Bader, 1991; Macchi & Sironi, 2003; Jena, 2013; Haberland, 2013), until the technical possibilities enabled the systematic physical-chemistry cluster generation. For this reason, the theory has played an important role in the development of cluster science. Since many cluster properties are not easily

measured directly from experiment, theoretical models and computational methods have been very useful in helping to interpret spectroscopic and mass spectrometric data (Johnston, 2002).

In the past 35 years, X-ray Absorption Spectroscopy (XAS) has proved to be an invaluable tool to study the electronic and structural properties of condensed matter systems (Van Bokhoven & Lamberti, 2016), and it is one of the most versatile and used techniques for the characterization of materials (Iwasawa *et al.*, 2017). Its low photoelectron energy part, X-ray Absorption Near-Edge Structure (XANES) as well as its extended part, Extended X-ray Absorption Fine Structure (EXAFS), are widely used for more than a decade for the characterization of clusters (Benfield *et al.*, 2001; Zhang *et al.*, 2007). XAS is submitted to transition rules, and its main dipole component obeying to $\Delta l = \pm 1$, makes that at the K-edge, the probed states are the *p* states whereas at the L23 edges, there are the *s* and *d* states. When the absorbing atom is a 3*d* transition element, such as copper, quantitatively it is mainly the $\Delta l = +1$ contribution which is seen, and so, the 3*d* states. Because p states are more delocalized than *d* states, their overlap with surrounding is stronger and consequently sensitivity of K edges to geometry is usually higher. On the contrary, the direct probe of the non-occupied 3*d* states makes the L23 edges directly sensitive to the projection of the partial density of state (DOS), onto the absorbing atom driving a lot of the physics of these systems. In this study, we thus use these complementary sensitivities making the analysis with both K and L3 Cu edge. Often used to study electronic and magnetic properties (Pearson *et al.*, 1993; Nesvizhskii & Rehr, 1999), the L23 edges can also be used, complementary to the K-edge for geometrical analysis. For example, Mazalova and Soldatov (Mazalova & Soldatov, 2008), analysing Cu L3 edges, have demonstrated that the icosahedral coordination is preferable for small copper clusters with respect to the cuboctahedral structure. It is known that the geometrical structure of copper nanoparticles changes with particle size because of the competition between surface and bulk energy contributions: icosahedral structure minimises surface energy whereas fcc structure minimises bulk energy (Peters, 2012). In other hand, in the case of very small Cu_{13} clusters, Soldatov et al. (2006) have demonstrated at the same edge that the contribution of non-constant potential in the interstitial regions (*i.e.* non muffin-tin potential) is extremely important. We thus have also performed simulations at the Cu L3 edge for the different cluster models.

Some authors argue that the structure is probably the most fundamental property of a cluster and it is important for understanding all aspects of chemical and physical behaviour (Doye & Wales, 1998; Bazin & Rehr, 2003) while others argue that it is the electronic structure (Ganteför *et al.*, 1995; Bonačić-Koutecký *et al.*, 2002). We will thus use in this context both absorption edges to get both kinds of information (Kau *et al.*, 1989).

The main purpose of our work is to gather theoretical means to produce simulated spectra corresponding to optimized clusters, which may serve as a basis to compare with spectra obtained experimentally. First, clusters are generated by an stochastic algorithm that combines the efficiency of

producing several stable clusters of fast simulated annealing (FSA) (Hohl *et al.*, 1988; Voskoboinikov *et al.*, 2008) with the accuracy of Density Functional Theory (DFT) to select, among them, the most stable ones (St-Amant & Salahub, 1990; Geerlings *et al.*, 2003; Seko *et al.*, 2009).

Second, Finite Difference Method Near Edge Structure (FDMNES) (Joly, 2001; Bunău & Joly, 2009; Joly *et al.*, 2009; Guda *et al.*, 2015) is a full potential DFT-LSDA code to calculate the XANES spectra from the atomic structures obtained in this case by the FSA-DFT optimizations. These spectra are then interpreted both in terms of the geometric configurations and in terms of the associated electronic configurations. A larger stability of Cu clusters with 20 atoms was found in comparison with those with 19 and 21 atoms. Based on this knowledge, we show the sensitivity of the XANES technique on the number of atoms n, (c.a 20), and on the morphology of the Cu_n nanoclusters.

In the next section we present the general methodology to generate the cluster geometry, and the way to simulate the XANES spectra. Section 3 presents the results and we discuss the information we get on the geometry and electronic structures.

2. Methodology

2.1. FSA and DFT strategies for the generation of clusters

Up to date, there is no exact technique to unequivocally find the most stable structure of a cluster. What it is possible, however, is to calculate with high precision the ground state energy of a given cluster structure. Thus, an elegant solution is to generate several stable clusters with a not so accurate but computationally fast technique, and later use a very precise tool to select the most stable structure among them.

Most search techniques create these candidates by random methods and later evaluate their stability using pair or many-body potentials. From the resulting 50 most stable structures, low-accuracy DFT minimizations are performed, followed by the selection of the 20 most stable, on which high-accuracy minimizations is performed.

Here, a similar approach was used. First, 5×10^3 clusters were randomly created from scratch. Then, fast simulated annealing (FSA) was performed on these structures. In the standard simulated annealing the temperature is slowly decreased so that the system has enough time to explore the free energy surface and finally get trapped in a few very stable configurations. In most cases, the structure with the global minima (according to the potential used) is found in this manner. In this case the temperature is decreased faster, so that the clusters can get trapped in configurations of local minima. Consequently, a large population of stable isomers with a wide range of stability is obtained, instead of a few very stable clusters. In contrast with other methods, here we used both, a pair potential (Lennard-Jones [LJ]) and a many-body potential (Embedded-atom method, [EAM]) to perform the FSA. The reason for this dual evaluation is that LJ favours structures with high coordination (pointing

towards molecular behaviour), while EAM favours structures with crystallographic arrangements (pointing towards a metallic bulk behaviour). By doing so, this unbiased search algorithm is nourished with two different criteria for stability, increasing the chances of finding stable clusters. After the FSA performed on 1×10^4 clusters (half with LJ, half with EAM), the 30 most stable structures were selected to run mid-accuracy DFT minimizations. From the resulting 16 most stable, high-accuracy DFT minimization were calculated.

DFT calculations were performed using the Quantum Espresso/PWSCF code (Giannozzi *et al.*, 2009). Vanderbilt ultrasoft pseudopotentials were used together with the Perdew-Burke-Ernzerhof (PBE) (Perdew *et al.*, 1996). A 32 Ry kinetic energy *cutoff* and a 320 ~ Ry charge density *cutoff* where used for middle-accuracy calculations, while for high accuracy calculations these parameters were chosen to be 42 Ry and 420 Ry, respectively. Only the Gamma point was considered in the electronic structure calculations. Geometry relaxations were converged when forces were less than 0.04 eV/Å and 0.01 eV/Å for middle and high accuracy calculations, respectively. Unit cells were big enough so that clusters were separated by at least 12 Å from their periodic images.

2.2. FDMNES strategies for the Cu K and L3 XANES simulations

The FDMNES code uses two DFT techniques to calculate the spectra, first the finite difference method (FDM) which is full potential and second the multiple scattering theory (MST) (Joly, 2001) using the so-called muffin-tin approximation on the potential shape which is faster, but also less precise. It is self-consistent (Bunău & Joly, 2009) and became recently highly faster when using FDM (Guda *et al.*, 2015).

Most often, K-edge simulations are performed considering the excited state of the absorbing atom with a core-hole and an extra electron in the first non-occupied state. From this, the potential is calculated and the Schrödinger or Dyson equations are solved to get the electronic structure of both the occupied and non-occupied states and further the spectrum. We have first checked that for these peculiar systems, the simulation using an absorbing atom in its ground state was very close to the ones calculated in the excited state. This approximation permits to calculate in one run the absorption spectra of all the site in the cluster (we will call this approach briefly as the *FDM-One-Run method*). Indeed, in the first part of the run the electron states are calculated and in the second part the direct projection of the electron states on the different absorbing Cu atoms gives the individual (but imbedded in the cluster) signals. The cluster signal is the simple sum on the different *n* Cu spectra. A convolution by a Lorentzian is in the last step, performed to take into account the finite life time of the core and photoelectron state.

On the basis of the structures obtained from the DFT minimization, the K and L3 edges are calculated using both MST and FDM.

Because, the code calculates first the electronic structure, it gives also the projection of the density of states on the different atoms. This projection can be partial giving thus the (l, m) states and further one can gets the HOMO-LUMO gaps.

3. Results and discussion

3.1. Generation of the clusters

From the 16 most stable clusters obtained from the high-accuracy DFT minimization, the three most stable isomers are shown in Fig. 1. The characterization of these structures is reviewed in Table 1.

Table 1 Relative energy (RE, in eV), formation energy (E_f, in eV), HOMO-LUMO gaps ($\Delta\varepsilon$, in eV), averaged coordination number (n_c), and Cu-Cu averaged bond length (R, in Å) of Cu_n with n = 19, 20 and 21. The formation energy (E_f) was taken as the energy difference with respect to the bulk structure, normalized over the total cluster atoms.

n	Isomer	RE	E_f	$\Delta\varepsilon$	n_c	R
	a	0.00	0.903	0.94	3.58	2.440
19	*b*	0.03	0.904	0.94	3.37	2.441
	c	0.07	0.906	0.94	4.42	2.455
	a	0.00	0.874	1.35	4.50	2.456
20	*b*	0.05	0.76	0.99	4.20	2.450
	c	0.23	0.885	0.79	4.40	2.454
	a	0.00	0.881	0.42	3.62	2.441
21	*b*	0.04	0.883	---	4.00	2.450
	c	0.04	0.883	---	4.19	2.452

Our results are in close agreement with previous systematic DFT Cu-CNs search. We found the same three most stable structures for Cu_{20} and Cu_{21} than those obtained with the basin-hopping (Jiang *et al.*, 2012), and the big-bang algorithm. The fact that using three different unbiased search algorithms the same three lowest-energy structures are found gives strong evidence that these structures are the most likely to be find in nature. We are not aware of other stable structure for Cu_{19} than that obtained by M. Yang *et al.* (Yang *et al.*, 2006). This structure appears to be our second most stable structure Cu_{19b}.

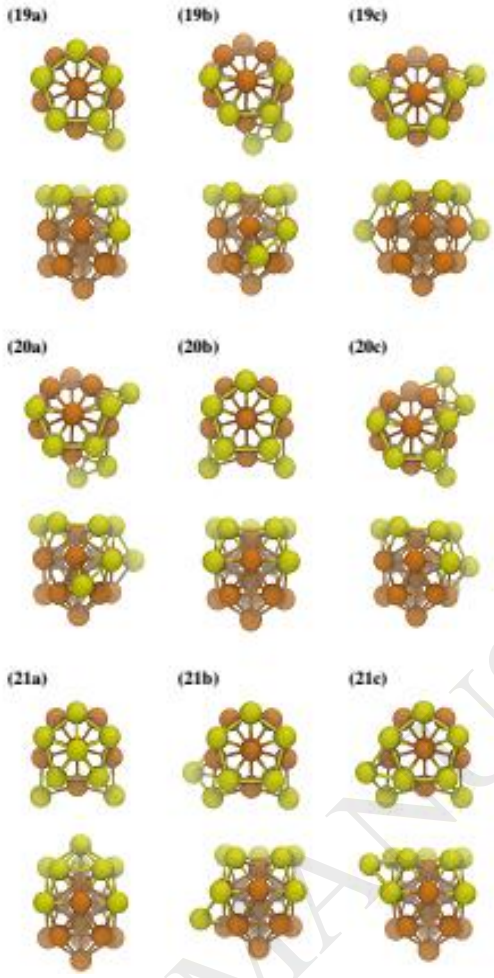

Figure 1 Top (above) and side views (below) of the most stable structures of Cu_{19}, Cu_{20}, and Cu_{21}. The isomers are shown in order of decreasing stability. The 13-atom icosahedral core is coloured orange, while the rest of the atoms are coloured yellow.

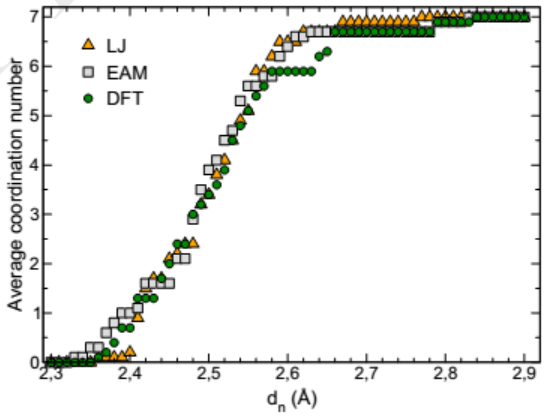

Figure 2 Average coordination number with respect to the first neighbour distance (d_n). Values were calculated for the most stable Cu_{20} cluster according to LJ, EAM, and DFT minimizations.

The coordination number n_c of a structure with N atoms is obtained by the sum of first neighbours of each atom, divided by N. Getting n_c for bulk metals is straightforward, since the distance of first neighbours d_n is the same for all the atoms. For clusters, however, first neighbours can be found at several different distances. Consequently, n_c will depend on which distance of first neighbours has been chosen. As an example, Fig. 2 shows the n_c as a function d_n for the Cu_{20} a structure minimized with LJ, EAM, and DFT. In this work the threshold distance was chosen to be 2.52 Å since it corresponds to a region of high slope in Fig. 2, which makes it useful to differentiate isomers with similar structures and/or similar Cu-Cu distances. Another important outcome of this figure, is that both potentials (LJ, and EAM) show a variation of n_c with respect to d_n that is in close agreement with DFT results. This suggests that the minimized structures of the candidates generated by these potentials are not far from that of DFT.

Concerning the relative stability of these clusters, it is well established that without geometric and/or electronic effects, the cluster stability should increase with the size due to a decrease of the surface energy. The electronic effect causes alternative jumps of stability as a function of cluster size. Alkali and noble metal clusters with even number of electrons are more stable than those with an odd number, due to the electron pairing effect (Yang *et al.*, 2006). This effect is particularly important in Cu_{20} due to a 20-electron shell-closing effect. This is also reflected in its high ionization energy (IP) in comparison with its two neighbours: 5.6 eV, 5.9 eV, and 5.1 eV for n = 19, 20, 21, respectively (Knickelbein, 1992). In order to have a more general picture of stability and the averaged coordination number of the most stable isomers, these parameters are correlated in Fig. 3.

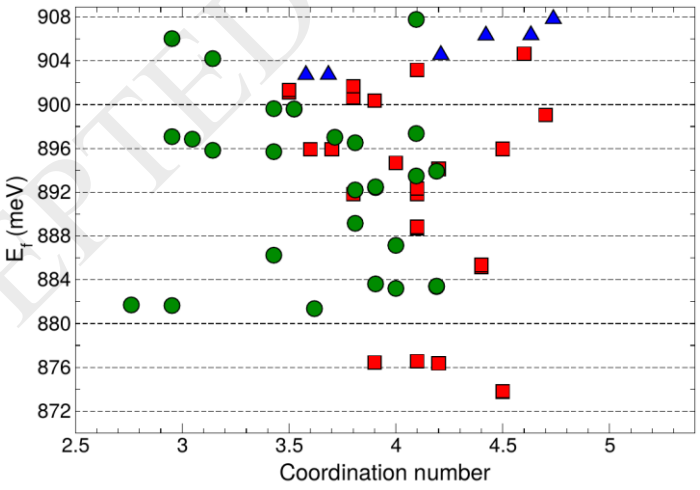

Figure 3 Formation energy of the most stable clusters found for Cu_n with n = 19, 20, and 21 (circle, square, and triangle, respectively) as a function of the coordination number.

This plot shows that for the threshold d_n chosen, the most sable clusters have a coordination number around 2.7 and 4.7. The four lowest-energy structures of Cu_{20} are even more stable than the most stable Cu_{21} structure. Another distinguishable feature of Cu_{20} is its relatively large band gap, especially for isomer 20*a*.

The usual way to get the band gaps is through the Band Structure (BS). In Figure 4 shows the BS for Cu, in which the differences come from the electronics of the system are clearly observed. In particular, both the Cu_{20} and the Cu_{21} show the greatest differences in relation to the morphological structure of the clusters. This may be relevant when interpreting the XANES spectra depending on the electronic structure.

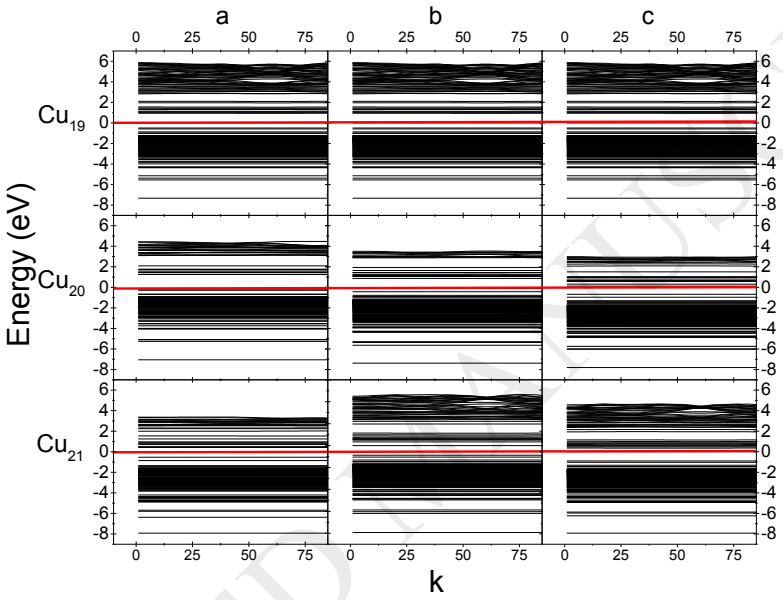

Figure 4 Band structure in function of wave vector k. The red line is for $E = 0$ eV (Fermi energy E_F).

3.2. XANES simulations

3.2.1. Cu K edge in bulk Cu

To get a reference in the simulation and to understand where the specific features in the spectra comes from, one first presents some results on the Cu metal cfc structure. FDMNES uses a cluster approach even for periodical system. The cluster, is built around a prototypical absorbing atom with a radius such as the projection of the electronic structure on the absorbing atom is nearly the same than in an infinite crystal. This is tested by increasing the radius R of the cluster up to convergence looking at the absorption spectrum shape. It is usually reached, in well-ordered material with R ≈ 7 Å. Results are shown Fig. 5 for MST (1) and FDM (2). From top to bottom R = 3 Å, 13 atoms (circle), R = 5 Å, 43 atoms (dash-dot),

and R = 7 Å, 135 atoms (black full line). The solid grey line corresponds to the experimental data for metallic copper.

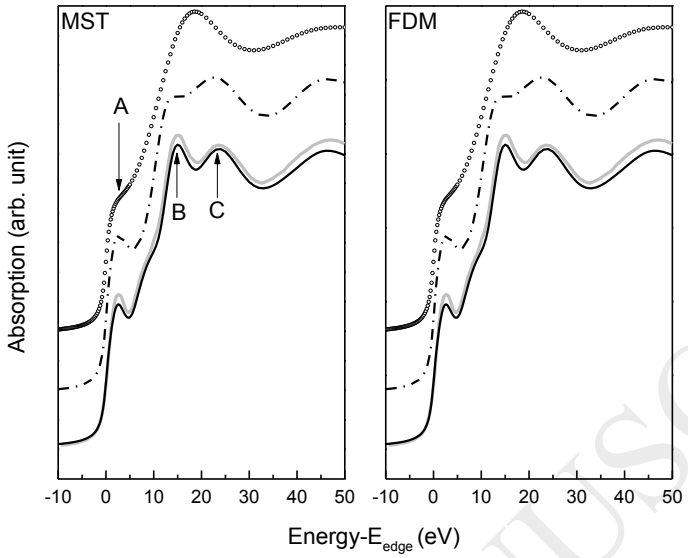

Figure 5 MST and FDM methods. Circle: radius 3 Å (13 atoms); dash-dot: radius 5 Å (43 atoms); black full line: radius 7 Å (135 atoms). Grey full line: experimental Cu K XANES for metallic foil. In both cases the calculation is non-SFC. E_{edge} = 8979 eV.

It is necessary to remark that in the works of Joly (2001) and Joly *et al.* (2009) are compared and analysed the simulation using MST and FDM.

We focus on some specific aspects. We can first remark that the observation of the splitting between B and C peaks appears with R ≥ 5 Å, while the peak A just needs one surrounding shell to be present. We take these features A, B and C as a general signature of bulk fcc copper but more specifically, we remember that the B-C splitting needs a rather long range order (Lytle *et al.*, 1988). The peak A is due to the transition 1s to 4p in the $3d^{10}$ configuration (Bazin & Rehr, 2003), as it is also reported in cluster's studies, from pioneering work (Apai *et al.*, 1979; Montano *et al.*, 1986) until more recent papers (Nguyen *et al.*, 2016; Huseyinova *et al.*, 2016).

3.2.2. Cu K edge in Cu-NCs

Fig. 6 shows the simulations of the different cluster models, Cu_{19}, Cu_{20} and Cu_{21} for MST method and FDM-One-Run method. The dash lines are indicative of the main characteristics of the simulated spectra.

We first note that the peak A appears weakly like a shoulder in the MST simulation, showing the necessity of the full potential approach as done in FDM. It is expected that lower density and lower symmetry make the muffin-tin approximation less good. In FDM-One-Run method, this peak is 30%

higher than in Cu bulk and shows a shoulder. We also note the energy shift of the maximum of this feature depending in the cluster model. If the Cu_{19} isomers do not mark so much differences, the Cu_{20} isomers show clearly a 2.2 eV splitting in the peak A, with a global higher intensity, the highest one being for the most stable Cu_{20a}. For Cu_{21}, the lesser stable isomers are similar, the most stable presents a slight energy shift and a larger splitting in the same feature A.

We thus remark a slightly higher sensitivity on the cluster shape than on the atomic numbers, but nevertheless note that the differences are relatively small between all these systems. This fact also explains why MST simulations are inappropriate.

The splitting B-C, typical of long range order arrangements, is not present in the simulated spectra by either of the two methods, which is consistent with the nature of the systems. A position difference is observed in the maximum, for the spectra simulated by MST method this position is close to 4 eV above the position of the maximum of the spectra obtained by FDM-One-Run method.

In another order, taking advantage of the fact that FDMNES code allows to compare the spectra which can be coming from two calculations, using the standard metric D_1, where D_1 is the strong integrated distance $D_1(f;g) = \frac{1}{2}\int|f(x) - g(x)|dx$, and *R-factor* (Zanazzi & Jona, 1977; Lindgren et al., 1984). The values obtained for D_1 and *R-factor* are summarizing in Table 2. D_{1ij} represents the metric between the spectrum *i* and the spectrum *j*.

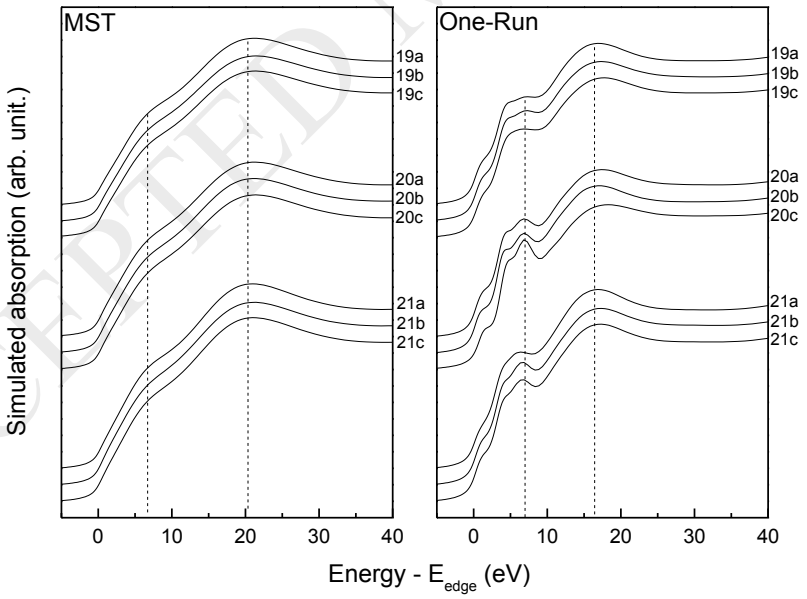

Figure 6 MST and FDM-One-Run methods for Cu_{nx}, with n = 19, 20 and 21, and x = a, b, or c. In all cases the calculation is non-SFC. E_{edge} = 8979 eV.

Table 2 Standard metric D_1 and *R-factor* obtained for comparison between two simulated spectra (K-edge).

	D_{1ab}	R_{ab}	D_{1ac}	R_{ac}	D_{1bc}	R_{bc}
Cu_{19}	0.53634	0.00033	0.53994	0.00045	0.36722	0.00024
Cu_{20}	0.45901	0.00035	0.57770	0.00041	0.41634	0.00024
Cu_{21}	0.86533	0.00086	0.48598	0.00032	0.48821	0.00031

We will compare these results with those obtained for simulations on the L3 edge (Table 3, in following pages).

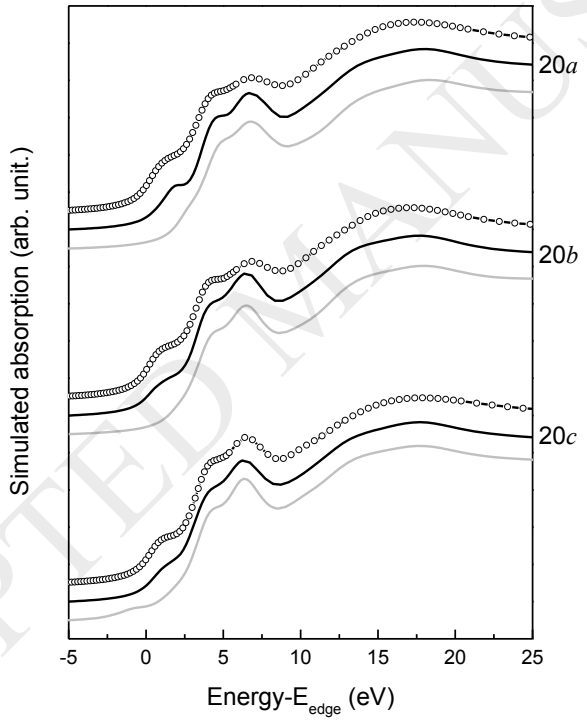

Figure 7 Comparison of the spectra generated by three different methods, FDM-One-Run (circle + line), FDM-nonSCF (full black line), and FDM-SCF (full gray line), for the system Cu_{20}. (E_{edge} = 8979 eV).

For completeness, and in order to show the benefits of the calculation using FDM-One-Run method, in Fig. 7 we see the comparison between the simulated spectra using the three methods: FDM-One-Run (circle + line), FDM-nonSCF (full black line), and FDM-SCF (full gray line). The first thing observed is a minimal difference between the spectrum calculated using FDM-One-Run versus the

spectrum calculated using FDM-nonSCF. The second is that in the simulated spectra by FDM-SCF disappears the first "shoulder" present in the spectra obtained by the other two methods. Beyond the disappearance of this "shoulder", there are no major differences between the three methods. From this perspective, and taking into account the great difference in calculation times, the use of the method is optimal. To put precise dimensions in relation to the times, the duration is about 1/20 and 1/23 for FDM-One-Run *vs.* FDM-nonSCF, and FDM-One-Run *vs.* FDM-SCF, respectively.

We see in Fig. 8 the Cu K XANES simulations for the first shells at central absorber Cu-atom in the metallic mesh. The emergence of the peak C (Fig. 5) comes with the increase of the number of atoms, Cu_{13}, Cu_{19}, Cu_{43} and Cu_{79}, respectively. In the Cu_{19} case, we note a splitting in the immediate post-edge region, weakly observed in any Cu_{19} clusters model.

At this point it becomes necessary to clarify that, unlike the cluster generated by modifying the radius (*i.e.*, the cluster is imbedded in the Cu bulk; see Fig. 5), the simulation was generated for the "naked" cluster obtained from the outputs-FDM calculus for the first neighbor spheres to the central atom. Due to this reason, qualitative differences are observed, for example, for Cu_{43} (R = 5 Å, in Fig. 5) and "naked"-Cu_{43} (Fig. 8). Moreover, in the latter case it was used FDM-One-Run method whereas in the first case (Fig. 5) was used FDM-nonSCF method for crystal structure.

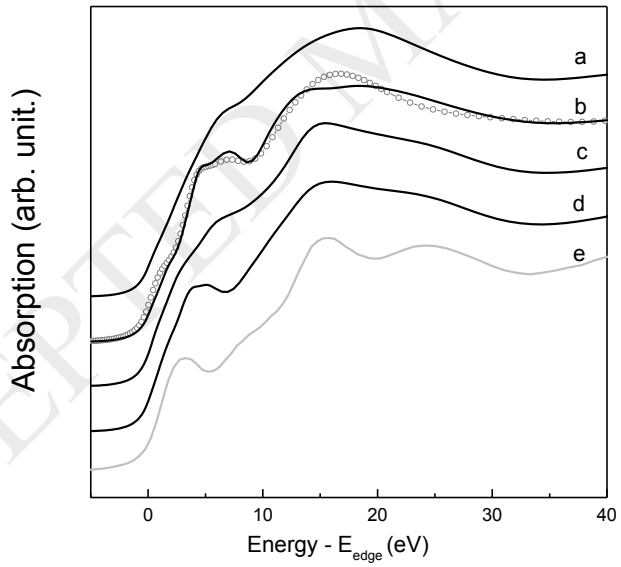

Figure 8 Cu K XANES simulations for the first shells at central absorber Cu-atom in the metallic mesh. a. First shell: Cu_{13}. b. Second shell: Cu_{19} in black (in open circle: Cu_{19a}). c. Third shell: Cu_{43}. d. Fourth shell: Cu_{79}. In grey (e), the Cu K XANES for Cu metallic.

3.2.3. Cu L3 edge in Cu-NCs

Figure 9 shows the experimental Cu L3 edge XANES for the Cu bulk system compared with the simulated spectra with nine Cu-CNs models.

We first observe a contribution of a bulk metal signal. Also note the more important difference between the different isomers for Cu_{20} and Cu_{21}, whereas for the Cu_{19} isomers these differences are not very appreciable. This fact can be related to what is observed in the Band Structure (Fig. 4), where there is no significant difference for the Cu_{19} isomers.

The white line intensity evidences a density of unoccupied 3*d* state. The number of unoccupied states is simply proportional to the area of the white line (Nesvizhskii & Rehr, 1999; Bazin & Rehr, 2003). The area of white line is obtained by simple integration between 925 and 933 eV. Through this method no significant differences in the level of occupation of the 3*d*-state are obtained, only the Cu metallic has an occupation of the order of 5% higher. Using FDMNES-code, the occupation of the 3*d*-level is calculated by integration up to a chosen atomic radius, here 1.1 Å. The average over all the cluster atoms gives 9.45_1, 9.50_1 and 9.50_1 respectively for Cu_{19a}, Cu_{19b} and Cu_{19c}. The white line changes for Cu_{21} are similar to the one for Cu_{19}, and the 3*d*-DOS given by the calculation, of the same order: 9.46_1, 9.50_1 and 9.48_1. In the case of Cu_{20}, unlike the previous two, the Cu_{20a} isomer has an intensity for white line greater than the Cu_{20b} and the Cu_{20c}. The respective values obtained were 9.48_1, 9.45_1 and 9.45_1.

It is worth taking note that we always get values less than 10. We must nevertheless take into account that the limit of the integration area is relatively arbitrary, but the variation versus the models is objective. We have also observed that the 3*d* occupancy rate is higher for the inner atoms at the cluster than those at the cluster border. For metallic Cu, where the Cu 3*d* band is supposed to be full, one gets 9.6 3*d*-electrons per Cu atom (Williams & Lang, 1978). This fact with the white line shape show the limit of the crude model with a 3*d* full system in the real situation, where in the continuum *n* is not anymore a good quantum number (Grioni *et al.*, 1989; de Smit *et al.*, 2010; Monte *et al.*, 2015).

We observe in the Fig. 9 that the general feature of the spectra, except for small shifts in the second peak (9.2 and 9.3; see the second vertical dashed-line), retain some the characteristics attributed to the metallic Cu.

Table 3 summarizes the values obtained for the D_1 metric and the *R-factor*. In all cases, with the exception of Cu_{19}-D_{1bc} and Cu_{21}-D_{1bc}, the values of D_1 and *R-factor* are greater by an order of magnitude in the comparison for the L3 edge *versus* the comparison on the K edge. This fact is indicative of a greater difference between the spectra. Because we compare spectra generated from the same number of atoms and whose only difference is the morphological structure in the arrangement of those atoms, it is possible to attribute that ordering is what produces the effects obtained on the spectra. Under this perspective, according to the metric used, it can be affirmed that Cu K-edge spectra is less sensitive to the geometrical parameters than the Cu L3-edge ones.

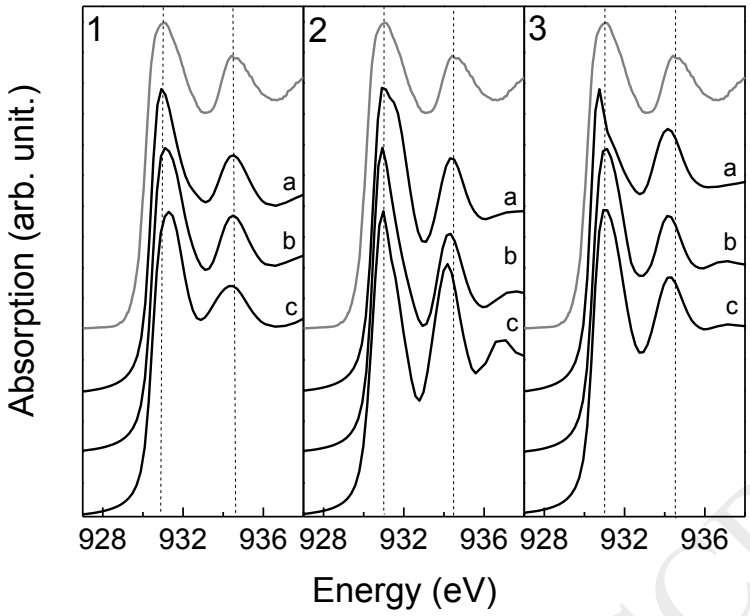

Figure 9 (1) Cu_{19}. (2) Cu_{20}. (3) Cu_{21}. In grey metallic bulk Cu (experimental data). In each frame, the spectra "a" correspond to Cu_{na}, "b" corresponds to Cu_{nb} and "c" corresponds to Cu_{nc}. In all cases the calculation is non-SFC.

Table 3 Standard metric D_1 and *R-factor* obtained for comparison between two simulated spectra (L3-edge).

	D_{1ab}	R_{ab}	D_{1ac}	R_{ac}	D_{1bc}	R_{bc}
Cu_{19}	0.99080	0.00190	1.12055	0.00314	0.60299	0.00081
Cu_{20}	1.27007	0.00445	4.45354	0.03184	5.21903	0.05262
Cu_{21}	1.47255	0.00727	1.39764	0.00742	0.26279	0.00014

3.2.4. HOMO-LUMO gaps obtained by FDMNES

As already stated above, the FDMNES code calculating first the electronic structure, it also gives the projection of the density of states on the different atoms. This projection can be partial giving thus the (l, m) states and further one can gets the HOMO-LUMO gaps (Guda *et al.*, 2015). In the Table 4 the results obtained are shown.

Now we obtain a minimum discrepancy with the obtained by DFT in this same work (see Table 1, Δε, HOMO-LUMO gaps). Usually, when the size of the cluster increases, the gap decreases. As a rule, DFT is known to yield underestimated quantitative values of the HOMO–LUMO gap, for the estimation of relative changes in the gap width of free clusters as the function of the size of clusters in

reference to the solid (Yalovega *et al.*, 2010). This would explain the small difference between the two methods, although the results obtained are convergent and of the same order.

Table 4 HOMO-LUMO gaps ($\Delta\varepsilon$, in eV) obtained by FDMNES.

	Cu_{19a}	Cu_{19b}	Cu_{19c}	Cu_{20a}	Cu_{20b}	Cu_{20c}	Cu_{21a}	Cu_{21b}	Cu_{21c}
$\Delta\varepsilon$ (eV)	1.10	1.05	1.10	1.50	1.15	1.10	0.70	0.70	0.75

The set of results obtained through the FDMNES simulations for a group of Cu-CNs obtained and optimized by FSA-DFT allow us to infer a series of novel conclusions for these systems. In particular, the 3*d*-state occupation obtained in combination with the gap is a manifestation of the non-metallic nature of these systems.

We believe that it is important to be able to establish solid knowledge about this type of systems whose first synthesis trials to produce naked clusters are performing in many chemical research laboratories at present. In this research we have seen, for example, that the Cu L3-edge is affected by the geometry of the system more than the Cu K-edge, which would indicate that it is preferable to perform studies in the region of lower energies to characterize this type of system.

4. Conclusions

We studied a set of Cu nanoclusters with 19, 20 and 21 atoms with three isomers in each case, generating the simulated spectra, which were compared with each other and with an experimental spectrum of stable Cu_n ($n \approx 20$) clusters.

We found, by FSA-DFT, an enlarged stability of Cu clusters with 20 atoms compare to the ones with 19 and 21 atoms. Particularly, the four lowest-energy structures of Cu_{20} are even more stable than the most stable Cu_{21} structure. Another distinguishable feature of Cu_{20} is its relatively large band gap (1.35 eV, *vs*. 0.94 eV for Cu_{19} and 0.42 eV for Cu_{21}). The electronic structure resulting from the *ab initio* XANES simulation, gives a partial 3*d* occupation of the order of 9.5 electrons per atom. We also found a HOMO-LUMO gap consistent with previous DFT simulations, that accounts for the non-metallic nature of these systems.

Surprisingly, we observed that the absorption Cu K-edge spectra, in the present studied cases, is less sensitive to the geometrical parameters than the Cu L_3-edge ones. We have demonstrated that the complementary analysis of K and L_3 spectra, using *ab initio* simulations, can give relevant

information on the cluster geometry and electronic structures, doing the presented methodology relevant for the study of nanometric systems.

Finally, we have used four XANES calculation methods for Cu K edge in this type of systems: MST method, FDM-One-Run method, FDM-nonSCF method, and FDM-SCF method. We observe that using the MST method there are no variations in the spectra despite the differences in the structures of the clusters. On the order hand, there are no significant differences between the spectra simulated by FDM-One-Run, FDM-nonSCF, and FDM-SCF, privileging FDM-One-Run over the other two methods due to the calculation time.

Acknowledgements L. Andrini thanks to CONICET by the partial financing of the stay for researchers developed in the Institut NEEL CNRS/UGA, Grenoble, France. L.A. and F.G. Requejo thanks to FONCyT PICT 2015-2285. M.M. Mariscal thanks the FONCyT PICT-2015-2191, CONICET PIP 11220110100992 and Universidad Nacional de Cordoba. M.M. Mariscal and G.J. Soldano thank the High Performance Computational Center (CCAD UNC) and the Texas Advances Computer Center (TACC) for access to supercomputers. The authors thank L.J. Giovanetti for Cu-Metallic L3 XANES measurements performed at the PGM beamline of the LNLS (Campinas, SP, Brazil).

References

Alivisatos, A. P. (1996). *J. Phys. Chem.* **100**, 13226–13239.

Apai, G., Hamilton, J. F., Stohr, J. & Thompson, A. (1979). *Phys. Rev. Lett.* **43**, 165.

Bader, R. F. (1991). *Chem. Rev.* **91**, 893–928.

Bazin, D. & Rehr, J. J. (2003). *J. Phys. Chem. B*. **107**, 12398–12402.

Benfield, R. E., Grandjean, D., Kröll, M., Pugin, R., Sawitowski, T. & Schmid, G. (2001). *J. Phys. Chem. B*. **105**, 1961–1970.

Bonačić-Koutecký, V., Burda, J., Mitrić, R., Ge, M., Zampella, G. & Fantucci, P. (2002). *J. Chem. Phys.* **117**, 3120–3131.

Bunău, O. & Joly, Y. (2009). *J. Phys. Condens. Matter*. **21**, 345501.

Calle- Vallejo, F. & Koper, M. (2013). *Angew. Chem.* **125**, 7423–7426.

Darby, S., Mortimer-Jones, T. V., Johnston, R. L. & Roberts, C. (2002). *J. Chem. Phys.* **116**, 1536–1550.

Doye, J. P. & Wales, D. J. (1998). *New J. Chem.* **22**, 733–744.

Ganteför, G., Cha, C.-Y., Handschuh, H., Icking-Konert, G. S., Kessler, B., Gunnarsson, O. & Eberhardt, W. (1995). *J. Electron Spectrosc. Relat. Phenom.* **76**, 37–45.

Garzón, I. L., Michaelian, K., Beltrán, M. R., Posada-Amarillas, A., Ordejón, P., Artacho, E., Sánchez-Portal, D. & Soler, J. M. (1998). *Phys. Rev. Lett.* **81**, 1600.

Geerlings, P., De Proft, F. & Langenaeker, W. (2003). *Chem. Rev.* **103**, 1793–1874.

Giannozzi, P., Baroni, S., Bonini, N., Calandra, M., Car, R., Cavazzoni, C., Ceresoli, D., Chiarotti, G. L., Cococcioni, M. & Dabo, I. (2009). *J. Phys. Condens. Matter*. **21**, 395502.

Grioni, M., Goedkoop, J. B., Schoorl, R., De Groot, F. M. F., Fuggle, J. C., Schäfers, F., Koch, E. E., Rossi, G., Esteva, J.-M. & Karnatak, R. C. (1989). *Phys. Rev. B*. **39**, 1541.

Guda, S. A., Guda, A. A., Soldatov, M. A., Lomachenko, K. A., Bugaev, A. L., Lamberti, C., Gawelda, W., Bressler, C., Smolentsev, G. & Soldatov, A. V. (2015). *J. Chem. Theory Comput.* **11**, 4512–4521.

Haberland, H. (2013). Clusters of atoms and molecules: theory, experiment, and clusters of atoms Springer Science & Business Media.

Haes, A. J., Chang, L., Klein, W. L. & Van Duyne, R. P. (2005). *J. Am. Chem. Soc.* **127**, 2264–2271.

Hohl, D., Jones, R. O., Car, R. & Parrinello, M. (1988). *J. Chem. Phys.* **89**, 6823–6835.

Huseyinova, S., Blanco, J., Requejo, F. G., Ramallo-López, J. M., Blanco, M. C., Buceta, D. & López-Quintela, M. A. (2016). *J. Phys. Chem. C*. **120**, 15902–15908.

Iwasawa, Y., Asakura, K. & Tada, M. (2017). XAFS techniques for catalysts, nanomaterials, and surfaces Springer.

Jena, P. (2013). Physics and chemistry of small clusters Springer Science & Business Media.

Jiang, M., Zeng, Q., Zhang, T., Yang, M. & Jackson, K. A. (2012). *J. Chem. Phys.* **136**, 104501.

Johnston, R. L. (2002). Atomic and molecular clusters CRC Press.

Joly, Y. (2001). *Phys. Rev. B*. **63**, 125120.

Joly, Y., Bunău, O., Lorenzo, J.-E., Galera, R.-M., Grenier, S. & Thompson, B. (2009). *Journal of Physics: Conference Series*, Vol. *190*, p. 012007. IOP Publishing.

Kaldor, A., Cox, D. M. & Zakin, M. R. (2009). *Advances*. 211.

Kau, L. S., Hodgson, K. O. & Solomon, E. I. (1989). *J. Am. Chem. Soc.* **111**, 7103–7109.

Kim, S.-W., Kim, M., Lee, W. Y. & Hyeon, T. (2002). *J. Am. Chem. Soc.* **124**, 7642–7643.

Kneipp, K., Wang, Y., Kneipp, H., Perelman, L. T., Itzkan, I., Dasari, R. R. & Feld, M. S. (1997). *Phys. Rev. Lett.* **78**, 1667.

Knickelbein, M. B. (1992). *Chem. Phys. Lett.* **192**, 129–134.

Lindgren, S. Å., Walldén, L., Rundgren, J. & Westrin, P. (1984). *Phys. Rev. B*. **29**, 576–588.

Lytle, F. W., Greegor, R. B. & Panson, A. J. (1988). *Phys. Rev. B*. **37**, 1550.

Macchi, P. & Sironi, A. (2003). *Coord. Chem. Rev.* **238**, 383–412.

Mazalova, V. L. & Soldatov, A. V. (2008). *J. Struct. Chem.* **49**, 107–115.

Montano, P. A., Shenoy, G. K., Alp, E. E., Schulze, W. & Urban, J. (1986). *Phys. Rev. Lett.* **56**, 2076.

Monte, M., Munuera, G., Costa, D., Conesa, J. C. & Martínez-Arias, A. (2015). *Phys. Chem. Chem. Phys.* **17**, 29995–30004.

Nesvizhskii, A. I. & Rehr, J. J. (1999). *J. Synchrotron Radiat.* **6**, 315–316.

Nguyen, T.-A. D., Jones, Z. R., Goldsmith, B. R., Buratto, W. R., Wu, G., Scott, S. L. & Hayton, T. W. (2015). *J. Am. Chem. Soc.* **137**, 13319–13324.

Nguyen, T.-A. D., Jones, Z. R., Leto, D. F., Wu, G., Scott, S. L. & Hayton, T. W. (2016). *Chem. Mater.* **28**, 8385–8390.

Oyanagi, H., Orimoto, Y., Hayakawa, K., Hatada, K., Sun, Z., Zhang, L., Yamashita, K., Nakamura, H., Uehara, M. & Fukano, A. (2014). *Sci. Rep.* **4**, Article number: 7199.

Pearson, D. H., Ahn, C. C. & Fultz, B. (1993). *Phys. Rev. B*. **47**, 8471.

Perdew, J. P., Burke, K. & Ernzerhof, M. (1996). *Phys. Rev. Lett.* **77**, 3865.

Peters, S. (2012).

Santiago González, B., Rodríguez, M. J., Blanco, C., Rivas, J., López-Quintela, M. A. & Martinho, J. M. G. (2010). *Nano Lett.* **10**, 4217–4221.

Schouten, K. J. P., Qin, Z., Gallent, E. P. & Koper, M. T. (2012). *J. Am. Chem. Soc.* **134**, 9864–9867.

Seko, A., Koyama, Y. & Tanaka, I. (2009). *Phys. Rev. B*. **80**, 165122.

Shao, Y., Molnar, L. F., Jung, Y., Kussmann, J., Ochsenfeld, C., Brown, S. T., Gilbert, A. T. B., Slipchenko, L. V., Levchenko, S. V., O'Neill, D. P., Jr, R. A. D., Lochan, R. C., Wang, T., Beran, G. J. O., Besley, N. A., Herbert, J. M., Lin, C. Y., Voorhis, T. V., Chien, S. H., Sodt, A., Steele, R. P., Rassolov, V. A., Maslen, P. E., Korambath, P. P., Adamson, R. D., Austin, B., Baker, J., Byrd, E. F. C., Dachsel, H., Doerksen, R. J., Dreuw, A., Dunietz, B. D., Dutoi, A. D., Furlani, T. R., Gwaltney, S. R., Heyden, A., Hirata, S., Hsu, C.-P., Kedziora, G., Khalliulin, R. Z., Klunzinger, P., Lee, A. M., Lee, M. S., Liang, W., Lotan, I., Nair, N., Peters, B., Proynov, E. I., Pieniazek, P. A., Rhee, Y. M., Ritchie, J., Rosta, E., Sherrill, C. D., Simmonett, A. C., Subotnik, J. E., Iii, H. L. W., Zhang, W., Bell, A. T., Chakraborty, A. K., Chipman, D. M., Keil, F. J., Warshel, A., Hehre, W. J., Iii, H. F. S., Kong, J., Krylov, A. I., Gill, P. M. W. & Head-Gordon, M. (2006). *Phys. Chem. Chem. Phys.* **8**, 3172–3191.

Smeeton, T. M., Kappers, M. J., Barnard, J. S., Vickers, M. E. & Humphreys, C. J. (2003). *Appl. Phys. Lett.* **83**, 5419–5421.

de Smit, E., de Groot, F. M., Blume, R., Hävecker, M., Knop-Gericke, A. & Weckhuysen, B. M. (2010). *Phys. Chem. Chem. Phys.* **12**, 667–680.

Soldatov, A. V., Yalovega, G. E., Masalova, V. L., Joly, Y., Adam, S., Lobo, A. & Möller, T. (2006). *Radiat. Phys. Chem.* **75**, 1519–1521.

Sönnichsen, C., Franzl, T., Wilk, T., Von Plessen, G. & Feldmann, J. (2002). *New J. Phys.* **4**, 93.

St-Amant, A. & Salahub, D. R. (1990). *Chem. Phys. Lett.* **169**, 387–392.

Toshima, N. & Yonezawa, T. (1998). *New J. Chem.* **22**, 1179–1201.

Van Bokhoven, J. A. & Lamberti, C. (2016). X-ray absorption and X-ray emission spectroscopy: theory and applications John Wiley & Sons.

Vilar-Vidal, N., Blanco, M. C., López-Quintela, M. A., Rivas, J. & Serra, C. (2010). *J. Phys. Chem. C*. **114**, 15924–15930.

Vilar- Vidal, N., Rey, J. R. & López Quintela, M. A. (2014). *Small*. **10**, 3632–3636.

Voskoboinikov, R. E., Osetsky, Y. N. & Bacon, D. J. (2008). *J. Nucl. Mater.* **377**, 385–395.

Wales, D. J. & Doye, J. P. K. (1997). *J. Phys. Chem. A*. **101**, 5111–5116.

Wales, D. J. & Scheraga, H. A. (1999). *Science*. **285**, 1368–1372.

Wang, J., Wang, G. & Zhao, J. (2002). *Phys. Rev. B*. **66**, 035418.

Wang, Y. & Herron, N. (1991). *J. Phys. Chem.* **95**, 525–532.

Williams, A. R. & Lang, N. D. (1978). *Phys. Rev. Lett.* **40**, 954.

Xie, J., Zheng, Y. & Ying, J. Y. (2009). *J. Am. Chem. Soc.* **131**, 888–889.

Yalovega, G. É., Shmatko, V. A. & Soldatov, A. V. (2010). *J. Struct. Chem.* **51**, 1070–1074.

Yang, M., Jackson, K. A., Koehler, C., Frauenheim, T. & Jellinek, J. (2006). *J. Chem. Phys.* **124**, 024308.

Zanazzi, E. & Jona, F. (1977). *Surf. Sci.* **62**, 61–80.

Zhang, J., Sasaki, K., Sutter, E. & Adzic, R. R. (2007). *Science*. **315**, 220–222.